Atomic Disorders Induced by Silver and Magnesium Ion Migrations Favor High Thermoelectric Performance in α-MgAgSb-Based Materials

Dandan Li, Huaizhou Zhao, Shanming Li, Beipei Wei, Jing Shuai, Chenglong Shi, Xuekui Xi, Peijie Sun, Sheng Meng, Lin Gu, Zhifeng Ren,* and Xiaolong Chen**

Thermoelectric devices can directly convert thermal energy to electricity or vice versa with the efficiency being determined by the materials' dimensionless figure of merit (*ZT*). Since the revival of interests in the last decades, substantial achievements have been reached in search of high-performance thermoelectric materials, especially in the high temperature regime. In the near-room-temperature regime, MgAgSb-based materials are recently obtained with *ZT* ≈ 0.9 at 300 K and ≈1.4 at 525 K, as well as a record high energy conversion efficiency of 8.5%. However, the underlying mechanism responsible for the performance in this family of materials has been poorly understood. Here, based on structure refinements, scanning transmission electron microscopy (STEM), NMR experiments, and density function theory (DFT) calculations, unique silver and magnesium ion migrations in α-MgAg$_{0.97}$Sb$_{0.99}$ are disclosed. It is revealed that the local atomic disorders induced by concurrent ion migrations are the major origin of the low thermal conductivity and play an important role in the good *ZT* in MgAgSb-based materials.

1. Introduction

The performance of thermoelectric materials is governed by its figure of merit $ZT = \left(S^2\sigma/\kappa\right)T$, where S, σ, κ, and T are the Seebeck coefficient, the electrical conductivity, the thermal conductivity, and the absolute temperature, respectively. Good thermoelectric materials possess the feature of "phonon glass, electron crystal."[1] The state-of-the-art strategies for improving *ZT*s for existing materials can generally be divided into two categories: one is to reduce the lattice thermal conductivity through nanostructuring or hierarchical architecturing;[2–4] the other is to enhance the electrical transport properties by resonant doping[5] or heavy band convergence.[6,7] Recently, narrow band semiconductors with intrinsically low lattice thermal conductivity caught intense interests in searching for new thermoelectric systems.[8–20] Two representative groups of materials: one possessing strong lattice anharmonicity, such as Zn_4Sb_3,[8] SnSe,[9] and the rocksalt I–V–VI$_2$ semiconductors (AgSbTe$_2$ and AgBiSe$_2$);[10,11] another being the so-called phonon-liquid electron-crystal (PLEC) materials, recently exemplified by Ag_2Se,[12] Cu_2Se,[13,14] Cu_2S,[15,16] and Cu_7PSe_6[17] that are expected to have ultralow thermal conductivity, favoring good thermoelectric performance. However, despite the subtle difference in the physical origins for the above two groups of materials in terms of their low lattice thermal conductivity, a common feature of weak chemical bonding exists in those compounds, which is well acknowledged. Thus, in general view of solid-state chemistry, the exploration of new thermoelectric materials within compounds that are associated with intrinsically weak chemical bonding would be a rational direction. Weak chemical bonding can be found in compounds with large-sized cages such as filled skutterudite,[21] layered structures such as Bi_2Te_3[3] and SnSe,[9] as well as those structures with distorted lattice.[2,8] α-MgAgSb has a distorted rocksalt lattice and shows superior thermoelectric properties, which has since received immediate research interest recently.[22–27]

α-MgAgSb with impurities was previously reported to have a $ZT \approx 0.5$ and very low thermal conductivity.[22] We adopted a two-step synthetic route and obtained pure phase. The chemical composition for the pure phase was identified to be close to MgAg$_{0.97}$Sb$_{0.99}$.[23] It is found that the Seebeck coefficient, the thermal conductivity, and *ZT* are enhanced in pure phase samples. Slightly Ni doping further enhances the thermoelectric performance with a peak $ZT \approx 1.4$, making it a very promising candidate to fill the gap in the *ZT* spectrum between low temperature $Bi_xSb_{2-x}Te_3$ alloy and middle temperature AgSbTe$_2$, PbTe-related materials, as shown in **Figure 1**a. Our most recent study has further demonstrated a record high thermal-to-electric energy conversion efficiency of 8.5% with the MgAgSb-based single-leg device.[27] Nevertheless, the structural and chemical origins behind the thermoelectric properties have not been fully understood. Here, in this paper, we present strong

D. Li, Prof. H. Zhao, S. Li, B. Wei, C. Shi, Prof. X. Xi, Prof. P. Sun, Prof. S. Meng, Prof. L. Gu, Prof. X. Chen
Institute of Physics
Chinese Academy of Sciences
Beijing 100190, P. R. China
E-mail: hzhao@iphy.ac.cn; chenx29@iphy.ac.cn

J. Shuai, Prof. Z. Ren
Department of Physics and TcSUH
University of Houston
Houston, TX 77204, USA
E-mail: zren@uh.edu

DOI: 10.1002/adfm.201503022

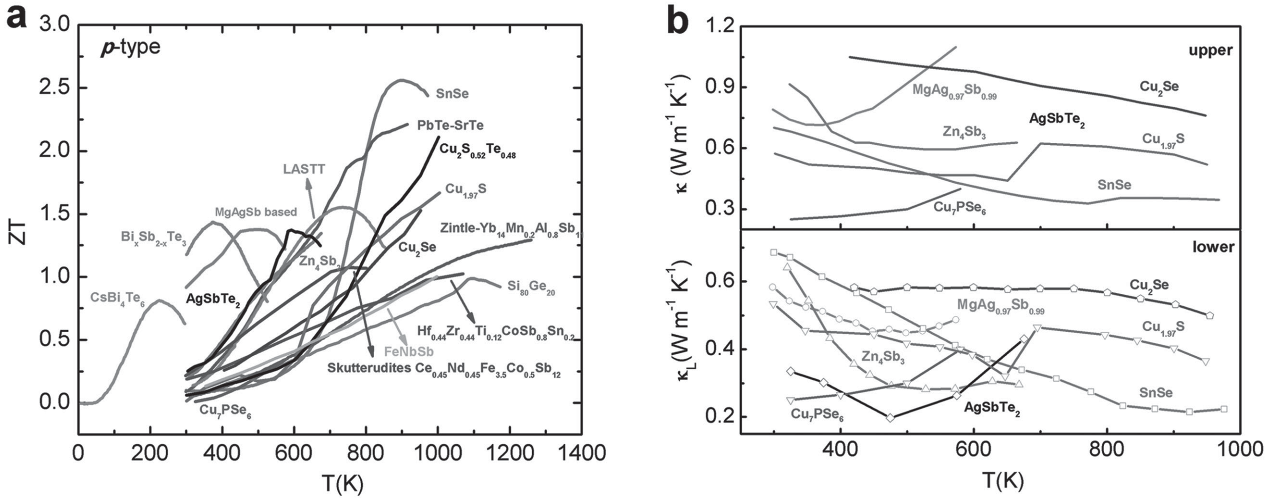

Figure 1. Thermoelectric properties of MgAgSb-based material in comparison with other materials. a) Ni-doped $MgAg_{0.97}Sb_{0.99}$ has peak $ZT \approx 1.4$ at 525 K, filling the gap between low temperature $Bi_xSb_{2-x}Te_3$ alloys and middle temperature PbTe-related materials in the ZT spectrum. b) Thermal conductivity of a few typical materials: upper panel shows a few thermoelectric materials having intrinsic low thermal conductivities; lower panel shows the corresponding lattice thermal conductivities to the upper materials. The related references to the data in the figure are listed as following: $Bi_xSb_{2-x}Te_3$,[3] PbTe-SrTe,[4] SnSe,[9] Cu_2Se,[13] $Cu_{1.97}S$,[15] $Cu_2S_{0.52}Te_{0.48}$,[16] Cu_7PSe_6,[17] skutterudites,[21] $MgAg_{0.97}Sb_{0.99}$,[23] $CsBi_4Te_6$,[36] $AgSbTe_2$,[37] Zn_4Sb_3,[38] LASTT,[39] $Yb_{14}Mn_{0.2}Al_{0.8}Sb_{11}$,[40] $Hf_{0.44}Zr_{0.44}Ti_{0.12}CoSb_{0.8}Sn_{0.2}$,[41] FeNbSb,[42] $Si_{80}Ge_{20}$.[43]

evidence that α-$MgAg_{0.97}Sb_{0.99}$ has weak chemical bonding and local structural disorder as manifested by the concurrent Ag^+ and Mg^{2+} ion migrations in the structure. Although the superionic-like conductivity has been identified in materials including Ag_2Se,[12] Cu_2Se,[13,14] Cu_2S,[15,16] Cu_7PSe_6,[17] etc., in which the cations have the liquid-like behavior of migrations in a stiffed framework built by corresponding anions, and this was believed to account for the low thermal conductivity in these materials. However, the ionic migrations in above materials are only referred to a single type of cations such as Cu^{2+} and Ag^+. For multiple element alloys, the simultaneous migration of two types of cations is rare.[28,29] The density function theory (DFT) calculations have been widely used to investigate the migrations of various types of ions in the field of ionic conductors,[30–32] while some preliminary experimental work related to the migrations of Ag^+ and Cu^{2+} cations in thermoelectric materials has been done.[33,34] The ion migration is believed to lead to the local atomic disorder (or partial liquid-like area in a crystal structure),[35] which is closely relevant to the low transverse phonon velocity, and account for the low lattice thermal conductivity in α-MgAgSb-based materials, as has been disclosed in other group of materials in Figure 1b. In addition, the considerable hole effective mass and moderate electrical transport properties also contribute to the exciting *ZT*s in MgAgSb-based materials. Our findings demonstrate that the local atomic disorder induced by the migration of Ag^+ and Mg^{2+} plays an important role in the *ZT* enhancement of MgAgSb-based materials and may help in developing new materials for thermoelectric applications.

Following the previous work,[44,45] Kirkham and Sharp proposed a series of structural models for MgAgSb through ab initio calculations, and assessed its thermoelectric properties.[20] According to ref.[23], the room temperature MgAgSb takes a tetragonal structure with lattice constants $a = 9.18$ Å and $c = 12.70$ Å and space group $I\overline{4}c2$. As shown in **Figure 2**a, Sb atoms actually form a fcc (face-centered cubic) closely packing sublattice, with Mg atoms lying in the centers of all the Sb octahedrons and Ag atoms half of the Sb tetrahedrons, which are connected each other by edge sharing and extended along the a, b, and c axis. We notice that the radius of Sb tetrahedron and octahedron are ≈0.55 Å and ≈1.01 Å, respectively, with the former being much smaller than the ionic radius of Ag^+ (≈1.26 Å) while the latter much larger than Mg^{2+} (≈0.66 Å). This is a very abnormal occupancy for Ag and Mg and the filled structure is expected to be unstable to some extent. On the other hand, the large difference in electronegativity between Mg (1.31) and Sb (2.05) results in strong bonding between Mg and Sb and form a rigid rock salt lattice, offsetting the distorted energy due to the size mismatch. The Ag atoms are positioned at the Mg–Sb cubes and the bonding with Sb is quite weak, implying the cohesive forces in MgAgSb lattice is very anisotropic and diverse.

2. Results and Discussion

We have performed an investigation on the variation of crystal structure vs. temperature for as-synthesized pure α-$MgAg_{0.97}Sb_{0.99}$. Figure 2b shows powder X-ray diffraction (XRD) patterns for as-synthesized sample at 305, 475, 570, and 610 K. Synchrotron X-ray diffraction (SXRD) was also carried out for the similar temperature range (Figure S2, Supporting Information), which is consistent with the regular XRD results. All of the peaks in the room temperature XRD pattern can be indexed based on the proposed tetragonal cell. As the temperature goes up to 475 K, a slight pattern shift to small angles can be observed due to lattice expansion as shown in Figure 2b. However, as indicated in the inset of Figure 2b, a few impurity

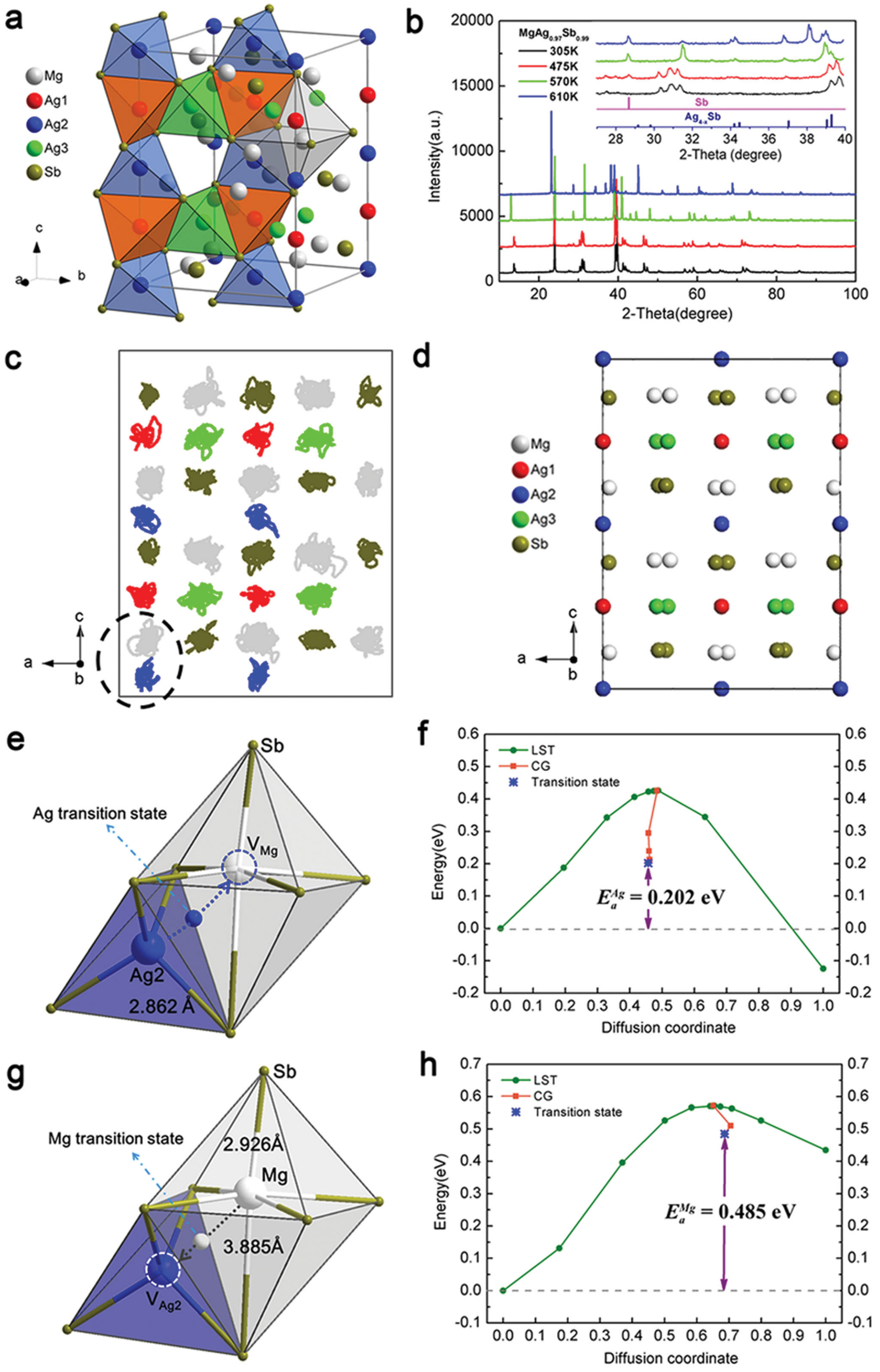

Figure 2. Crystal structure, temperature-dependent XRD patterns, MD simulation, and ion migration model in α-MgAg$_{0.97}$Sb$_{0.99}$. a) the crystal structure of α-MgAgSb proposed by Kirkham et al., b) temperature-dependent powder XRD patterns for as-synthesized MgAg$_{0.97}$Sb$_{0.99}$ from 305 to 610 K, c) trajectory of atoms in the a–c plane from MD simulation at 1000 K, d) corresponding crystal structure of α-MgAgSb in a–c plane for MD simulation, e) Ag^{+} migration model from Ag site to Mg vacancy in α-MgAgSb, f) activation energy and energy variation along the pathway of Ag migration under nonequilibrium state, g) Mg^{2+} migration model from Mg site to Ag vacancy in α-MgAgSb, h) activation energy and energy variation along the pathway of Mg migration under nonequilibrium state.

Table 1. The activation energy for Ag^+ and Mg^{2+} ion migrations in α-MgAgSb-based on DFT calculations.

Diffusion pathway	Activation energy [eV]	
	$DMol^3$	CASTEP
$Ag1 \rightarrow V_{Mg}$	0.547	0.358
$Ag2 \rightarrow V_{Mg}$	0.202	0.287
$Ag3 \rightarrow V_{Mg}$	0.192	0.226
$Mg \rightarrow V_{Ag1}$	0.678	0.523
$Mg \rightarrow V_{Ag2}$	0.485	0.386
$Mg \rightarrow V_{Ag3}$	0.577	0.454
$Ag1 \rightarrow V_{Ag2}$	–	0.740
$Ag2 \rightarrow V_{Ag3}$	–	1.950
$Ag3 \rightarrow V_{Ag1}$	–	1.124

peaks located at $2\theta = 28.77°$ and $36.95°$ emerge at this temperature, and these peaks can be attributed to Sb and $Ag_{4-x}Sb$ phases. When temperature is increased to 570 K, the main phase changes to β-MgAgSb structure with the same impurity Sb and $Ag_{4-x}Sb$ still being present, but in a larger amount than that in 475 K. Then at 610 K, all main diffractions can be indexed to γ-MgAgSb structure, while the amounts of Sb and $Ag_{4-x}Sb$ impurities increased to its highest level. The observation of the three polymorphs for MgAgSb has been previously reported by Kirkham et al.[20] However, it is rather interesting to see the constituent Ag and Sb dissociation from the host $MgAg_{0.97}Sb_{0.99}$ lattice with increasing temperatures. Since there are no Mg-related phases as impurity in the three XRD patterns shown above, we believe that this is a partial dissociation process. We speculated that owing to the lattice inhomogeneity in α-$MgAg_{0.97}Sb_{0.99}$, the lattice vibration might be accompanied by ion migration and this would lead to a breaking of chemical bonding between Ag and Sb at elevated temperatures. Thus inspired by the super ionic conductivity in Ag_2Se, Ag_2Te, and other Ag ion conductors,[12,46] and Mg^{2+} migrations in some ion conductive materials,[47] we performed the molecular dynamics (MD) simulations to investigate the migration of atoms in α-MgAgSb.

Figure 2c shows the MD-simulated trajectory of atoms in the x–z plane of α-MgAgSb at 1000 K. Here, the simulation temperature was used to scale up the velocities of atoms and cannot be viewed as the real temperature performed on α-MgAgSb. Figure 2d is the corresponding crystal structure of α-MgAgSb viewing along the b-axis. Collapse of structure has not been observed during the MD simulation. The large displacement of atoms in Figure 2c from their equilibrium positions implies that the atoms are weekly bounded, which are consistent with the appearance of phase dissociations as shown in the temperature-dependent XRD patterns. Interestingly, the trajectories of Ag (blue) and Mg (white) atoms shown in the black circles in Figure 2c are connected and tend to be overlapped with extended displacement, thus indicating that local concurrent migration between Ag and Mg atoms could probably happen. This further inspired us to perform the DFT calculations to investigate the all possible migrations that might happen in α-MgAgSb. The calculated activation energy for all possible ion migrations is shown in **Table 1**.

It is observed that the activation energy values for migrations among all three Ag sites are between 0.72 and 1.95 eV, which is much larger than those values (≈0.2 eV) in well-known Ag ion conductors, and also excludes the migration between different Ag sites in α-MgAgSb. However, to our surprise, the activation energy of migrations between three Ag sites and the Mg site is as low as those reported in Mg^{2+} and Ag^+ ion conductors,[48,49] which strongly supports the assumption of mutual ion migration between Ag and Mg in α-MgAgSb. As a representative, Figure 2e shows the migration pathway from Ag at the 4b site (Ag2) to an adjacent Mg vacancy in α-MgAgSb. It is noted that the atom Ag2 is initially located at the center of the Sb tetrahedron with the bond length of 2.862 Å, and the Mg vacancy is in the distorted Sb octahedron. Figure 2f shows the position-dependent energy variations for the Ag along the pathway of migration. The activation energy of migration is determined by the energy difference between the transition state and the initial state. Here, the total energy of the initial state is set to be 0 eV, so the activation energy for Ag^+ migration from Ag2 site to the Mg vacancy is obtained as 0.202 eV. Identically, the activation for Mg^{2+} migration from Mg site to the Ag2 vacancy is obtained as 0.485 eV. It is worth pointing out that the final energy of Ag and Mg migrations only refers to the nonequilibrium energy state during the migrations, and cannot be viewed as a final energy state in thermodynamics. In order to confirm the results of calculations of the energy variations associated with the Ag^+ and Mg^{2+} ion migrations, both programs of $DMol^3$ and CASTEP are used in our calculations, and the results are found to be rationally consistent. This reveals a unique type of ion migration between Ag site and Mg site in α-$MgAg_{0.97}Sb_{0.99}$.

The structure refinement for the XRD patterns of the as-synthesized and heat-treated α-$MgAg_{0.97}Sb_{0.99}$ samples based on the Rietveld method confirms the conclusions that we have obtained from the above DFT calculation. Figure S3 (Supporting Information) shows the structure refinement for these two XRD patterns based on the structure model proposed by Kirkham et al.[20] In Figure S3a (Supporting Information), the structure refinement against the XRD pattern of as-synthesized α-$MgAg_{0.97}Sb_{0.99}$ converges to $R_{wp} = 5.20\%$, $R_{exp} = 3.65\%$ and $\chi^2 = 2.03$, indicating the structural refinement is highly reliable. The results of refinement can be seen in Table 1S (Supporting Information). It is found that Ag vacancies exist in three Wyckoff sites, and the total Ag occupancy is 0.97, total Sb occupancy is 0.99, which are consistent with sample's nominal composition $MgAg_{0.97}Sb_{0.99}$. Antisite between Mg and Ag happens with a rough ratio of ≈3%, which is coincident with the conclusions from our calculation, experimentally evidenced the fact of ion migration between Ag site and Mg site in α-$MgAg_{0.97}Sb_{0.99}$. Moreover, the refined isothermal parameters show abnormally large value for the Mg site in the distorted Sb octahedral, which reveals the more active motions at this position than others. After the as-synthesized $MgAg_{0.97}Sb_{0.99}$ sample was heat treated at 575 K and quenched to room temperature, we did immediate XRD measurement and its structure refinement is shown in Figure S3b (Supporting Information).

The refinement shows that occupancies of Ag and Sb were 0.94 and 0.98 in the main phase, respectively, and antisite occupancy between Mg site and Ag site was also revealed but without significant increase comparing to that in as-synthesized sample.

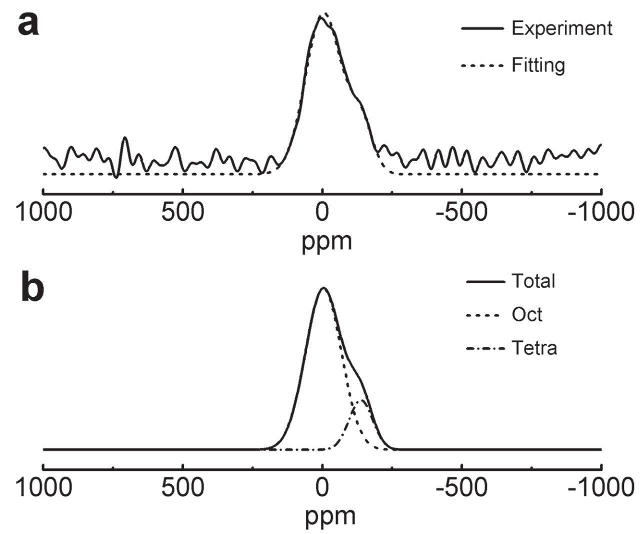

Figure 3. a) Static solid-state ^{25}Mg NMR spectra of as-synthesized α-MgAg$_{0.97}$Sb$_{0.99}$ sample, the black solid line refers to the experimental result and the gray dashed line refers to the fitting lines, respectively. b) Fitting details of the spectra reveal two central lines corresponding to two distinct local environments of Mg nuclei.

Considering the observed Sb and Ag$_{4-x}$Sb impurity peaks in the XRD patterns (Figure 2b), the refined composition MgAg$_{0.94}$Sb$_{0.98}$ is reasonable. As the DFT calculation shows, mutual ion migration for Ag$^+$ and Mg^{2+} in α-MgAgSb-based materials could be further facilitated with the increase of temperature, and bond breaking could happen between Mg–Sb and Ag–Sb, thus leading to the appearance of Sb and Ag$_{4-x}$Sb impurities. However, it is noted that the impurity will solvate themselves into the lattice after annealing at room temperature for 7–10 d, as shown in Figure S3 (Supporting Information), indicating the phase pure α-MgAg$_{0.97}$Sb is thermodynamically favorable.

^{25}Mg NMR experiment was performed to investigate the local environments of Mg atoms as shown in **Figure 3**a. Only narrow asymmetric central transition lines can be observed. For a deeper understanding of the local electronic structure, NMR CASTEP[50] and DMFIT program[51] were employed to analyze the linewidth and peak position. For the ^{25}Mg isotope at a distorted octahedral site in α-MgAg$_{0.97}$Sb$_{0.99}$ as indicated from previous XRD refinement, the calculated quadrupolar coupling constant is 2.88 MHz. The observed full line width at half magnitude is only 4 kHz, much less than the calculated one ($\approx$15 Hz) from second-order quadrupolar interactions. The absence of quadrupolar interactions indicates significant motional narrowing, in good accordance with active motions revealed from the above diffraction methods (Figure 2b). Two Gaussian lines were used to fit the spectra, as shown in Figure 3b. We consider the higher peak with $\approx$3.7 kHz linewidth at –4 ppm, which has 83% intensity in the spectra, corresponds to the Mg atoms in distorted Sb octahedron in α-MgAgSb structure. Meanwhile the smaller peak at –138 ppm with $\approx$2.45 kHz linewidth corresponds to the Mg atoms in Sb tetrahedron in α-MgAg$_{0.97}$Sb$_{0.99}$ structure. This assignment is consistent with the antisite occupations between Ag and Mg in the structural refinement for α-MgAg$_{0.97}$Sb$_{0.99}$ discussed above.

Scanning transmission electron microscopy (STEM) images were shown in **Figure 4**, which unambiguously show the existence of local disorder in α-MgAg$_{0.97}$Sb$_{0.99}$ sample. Figure 4a shows the atomic structure in the selected area of the α-MgAg$_{0.97}$Sb$_{0.99}$ specimen, which is viewed along the [0 1 –1] zone axis in the crystal structure. Figure 4b shows the expended region from Figure 4a, in which the atomic structure projecting along [0 1 –1] orientation matches very well with the atomic positions of Mg, Ag, and Sb in the structure model of α-MgAgSb. High-angle annular dark-field (HAADF) and annular bright-field (ABF) images were taken to further study the local disorder of atoms in α-MgAg$_{0.97}$Sb$_{0.99}$. Figure 4c shows the HAADF image. Notably, along the [0 1 –1] zone, the Ag and Sb atomic columns are partial mixed while Mg column is clearly visible.

Figure 4e shows the corresponding intensity line scanning along the blue line marked in Figure 4c. The peaks up towards in Figure 4e correspond to the Ag and Sb atomic columns. The valley in the red circle corresponding to Mg atomic column is found to be higher than the next nearest one, which indicates that other heavy atoms may move to Mg site. Figure 4d presents the ABF image from which the light element Mg can be readily captured. Figure 4f shows the corresponding intensity line scanning of Figure 4d. Contrary to the HAADF, the peaks up-wards represent the Mg atomic columns in ABF intensity line scanning. It is noted that the peak intensity in the red circle appears much lower than the others. This clearly indicates that there are other heavier atoms moving to this region, which could reduce the peak intensity, and the Ag atoms located in adjacent to Mg atoms could be responsible for this. In addition, the regions marked in red circle in the inset of Figure 4d appear darker than other normal position, indicating the Ag ion migrations to the Mg site from its own sites. Although the TEM did not offer the direct evidence of ion migration, the observation of local atomic disorders is a supporting evidence of ion migration.

The thermoelectric properties were found to be consistent with the structural evolution shown in Figure S3 (Supporting Information). **Figure 5**a shows the temperature-dependent electrical resistivity from 11 to 550 K. Filled blue squares indicates measured data for as-synthesized MgAg$_{0.97}$Sb$_{0.99}$ sample, and filled red circles represent resistivity for the heat-treated MgAg$_{0.97}$Sb$_{0.99}$ sample.

The solid line represents data from our previous work, which matches to the heat-treated sample.[23] Overall, the temperature-dependent resistivity shows a metallic behavior below 350 K. Considering the carrier concentration remains to be nearly constant at low temperatures (Figure S4, Supporting Information), we ascribe this behavior to the decrease in carrier mobility induced by the acoustic phonon scattering and defects scattering. The resistivity starts to decrease at around room temperature, which is consistent with the turning point in the Seebeck coefficient in Figure 5b due to bipolar effect. In the temperature region between 11 and 400 K, the as-synthesized sample shows higher resistivity than that of heat-treated sample. To get more understanding on the electrical properties, the room temperature Hall measurement was double checked by the Accent HL5500 Hall System for both samples. Room temperature Hall measurement shows that the latter

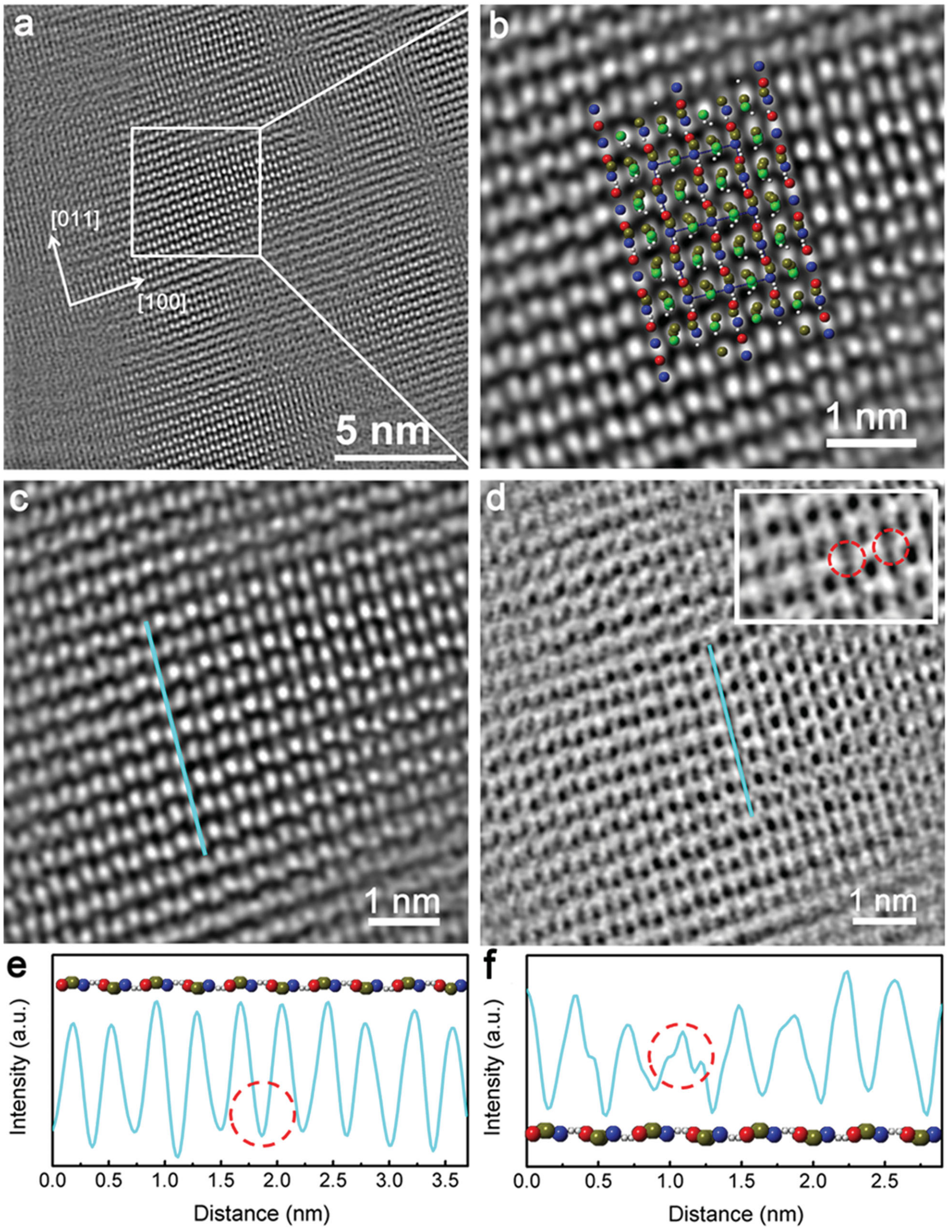

Figure 4. STEM images of $MgAg_{0.97}Sb_{0.99}$ samples aligned along the [0 1 −1] zone axis. a) TEM image of the atomic structure of the selected area of α-$MgAg_{0.97}Sb_{0.99}$, b) The comparison between the HRTEM atomic structure in the expended area of Figure 4a and the structure model along the [0 1 −1] axis for α-MgAgSb, c) HAADF image, d) ABF image, e,f) the corresponding intensity line scanning for HAADF and ABF images, respectively.

has higher hole concentration of 4.0×10^{19} cm^{-3}, almost doubled that of the as-synthesized sample 2.2×10^{19} cm^{-3}, with the mobility increasing from 71 to 76 cm^2 V^{-1} s^{-1} after heat treatment, which implies that the mobility of hole was not influenced by the structural defects induced by heat treatment. Taking into account the additional Ag and Sb vacancies in the heat-treated $MgAg_{0.97}Sb_{0.99}$ sample, which is refined to have the nominal composition of $MgAg_{0.94}Sb_{0.98}$ in Table S1 (Supporting Information), we ascribe the increase of hole concentration in $MgAg_{0.94}Sb_{0.98}$ to the presence of additional Ag^+ vacancies, regardless of the possible rise of minor electron carrier by the additional Sb^{3-} vacancies due to requirement of valance balance. The impurity Sb and $Ag_{4-x}Sb$ in the heat-treated sample might have complex, but minor contributions to the charge carriers. At higher temperature $T > 400$ K, there is no difference on resistivity between two samples because impurities start to emerge at around 400 K, which imply that both samples have the same composition of phase and impurities.

Temperature dependence of the Seebeck coefficient is shown in Figure 5b. The peak positions are located at around 325 k for both curves, while as-synthesized sample has higher Seebeck values below 350 K, which is consistent to its lower carrier concentrations, given the assumed single parabolic band model. The estimated bandgap E_g was ≈0.16 eV,[23] larger than the gap value

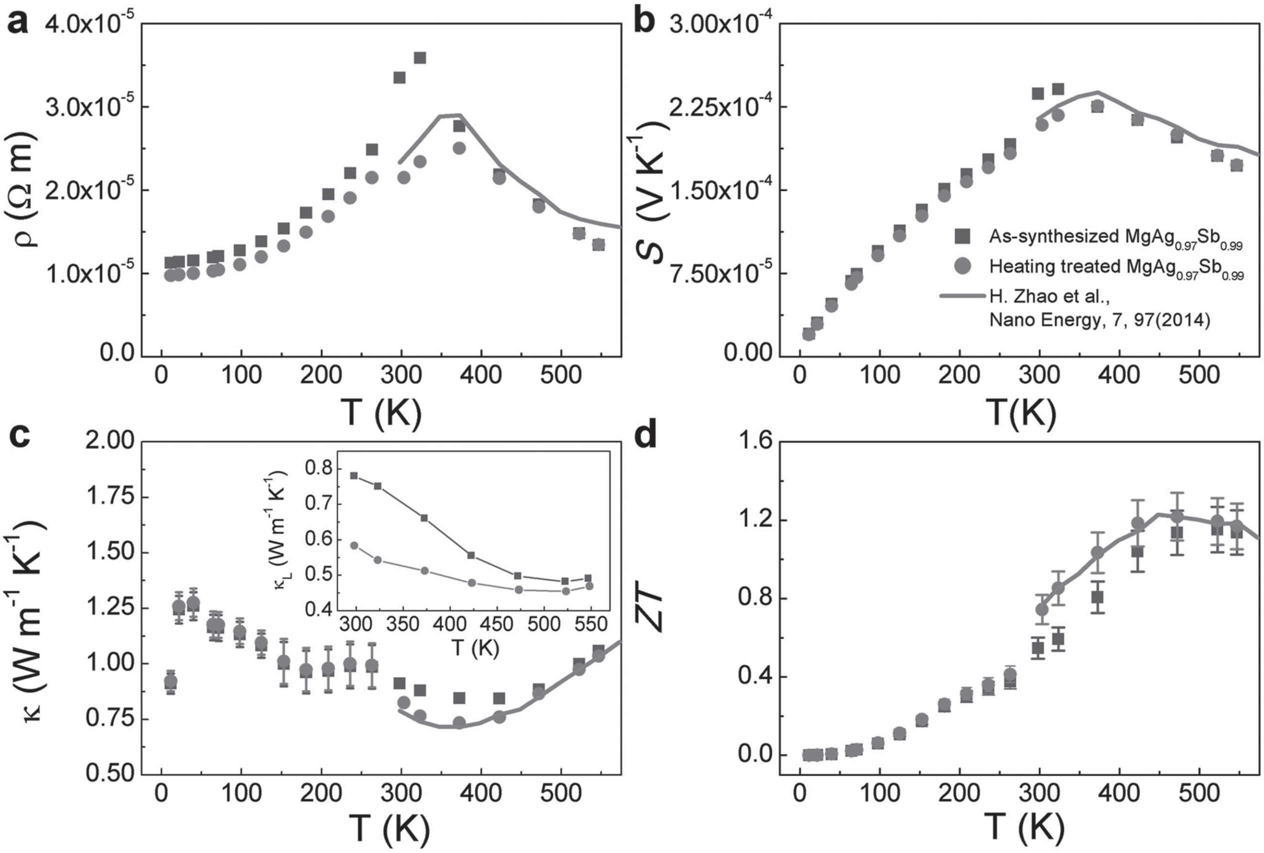

Figure 5. Temperature-dependent thermoelectric properties of the as-synthesized (square) and heat-treated (circle) α-MgAg$_{0.97}$Sb$_{0.99}$ samples from 11 to 550 K. a) Electrical resistivity, b) Seebeck coefficient, c) total thermal conductivity and lattice thermal conductivity (inset), d) figure-of-merit *ZT*s. Solid curves represent our reported data.[23]

of 0.063 eV between the valence band maximum at the X point and the conduction band minimum at the G point calculated by DFT (Figure S5, Supporting Information). This discrepancy is a common problem for DFT bandgap calculations with local density approximations. We estimate the hole effective mass using a single parabolic band model with acoustic phonon scattering, where the Seebeck coefficient in this model can be expressed as:[52]

$$S = \pm\frac{k}{e}\left\{2\frac{F_1(\xi)}{F_0(\xi)} - \xi\right\} \tag{1}$$

here ξ is the reduced Fermi level and F_x the Fermi integral of order x. Using the same formalism, the carrier concentration P can be expressed as:

$$P = \frac{4}{\sqrt{\pi}}\left(\frac{2\pi m^{*}kT}{h^{2}}\right)^{3/2} F_{1/2}(\xi) \tag{2}$$

here m^* is the effective mass and T is the absolute temperature. The Fermi level can be deduced from the experimental Seebeck coefficient in Equation (1) together with experimental hole concentration, the effective mass can be calculated from Equation (2). For the as-synthesized MgAg$_{0.97}$Sb$_{0.99}$, we calculated a hole effective mass of 1.36 m$_0$, while for the heat-treated MgAg$_{0.97}$Sb$_{0.99}$ m* is 1.63 m$_0$. In addition, the high mobility in α-MgAg$_{0.97}$Sb$_{0.99}$ is believed to be beneficial for its good electrical transport properties.

Temperature-dependent thermal conductivity is shown in Figure 5c. At low temperature, the thermal conductivity of heat-treated sample is slightly higher than that of the as-synthesized one, which is consistent with the increased electrical conductivity as shown in Figure 5a, and in turn the increased electrical thermal conductivity for heat-treated sample. However, it is in reverse trend with the decreased lattice thermal conductivity in the heat-treated sample due to increased phonon scattering by the emerges of defects and impurities in this sample, as shown in the inset of Figure 5c, which is supposed to lower the total thermal conductivity. Overall, both effects appear to compensate with each other, leading to subtle difference on their total thermal conductivities. It is also noted that there is a platform in the thermal conductivity in the temperature range 150–300 K, which is supposed to decrease with the increase of temperature and be consistent with its trend at elevated temperature. The radiation loss during the thermal conductivity measurement using PPMS may play the key role for this, and this would lead to the appearance of a small downturn in the *ZT* curve near 300 K (Figure 5d) from PPMS measurement. The two samples show significant difference on thermal conductivity in the temperature range of 250–500 K, which is believed to originate from the increased phonon scattering by the emerged defects and impurities in the heat-treated sample, inducing additional suppressions on thermal conductivity for this sample. When the temperature is higher than 450 K, both samples tend to have the same composition of phase and impurities, thus both thermal conductivity start to agree with each other. As we have reported recently,[23] heat-treated $MgAg_{0.97}Sb_{0.99}$ shows a very low thermal conductivity in the temperature range of 300 to 575 K. A maximum $\kappa \approx 1.25$ W m^{-1} K^{-1} can be found at 40 K. Unlike the temperature independent lattice thermal conductivity in $AgSbTe_2$[37] and the PLEC materials Cu_2Se,[13,14] Cu_2S,[15,16] Cu_7PSe_6[17] due to highly disordered Cu ions, the temperature-dependent κ for $MgAg_{0.97}Sb_{0.99}$ follows the $\kappa \approx \exp(\theta/T)$ law between 40 and 185 K. This indicates Umklapp scattering to be the major scattering mechanism, as can be seen in most of the crystalline solid materials,[49] similar to the case in SnSe.[9] This further suggests that α-$MgAg_{0.97}Sb_{0.99}$ still stand for a rigid crystal structure, irrespective of the low activation energy for Ag^+ and Mg^{2+} ion migration as found in Ag^+ and Cu^{2+} superionic conductors.[33,34] It is less likely that the concurrent ion migrations in α-MgAgSb would have to possess all the behavior of lattice thermal conductivity that the ionic conductors usually exhibit, i.e. temperature independent κ_L, depending on the species and mobility of the migrating ions in the materials. We believe that ion migrations in α-MgAgSb structure would lead to strong phonon scatterings and reduced lattice thermal conductivity in this material as ionic conductor thermoelectric materials usually have done. This discovery would enrich our knowledge on the mechanism of low thermal conductivity in other similar ion migration materials. The increase of thermal conductivity at 400 K is due to the bipolar effect, in agreement to the behavior of temperature-dependent electrical resistivity.

Ultrasonic measurements of the longitudinal and transversal phonon velocities were performed at room temperature. The longitudinal and transversal phonon velocities were found to be $v_l = 3708$ m s^{-1} and $v_t = 1120$ m s^{-1}, respectively. The mean phonon velocity v_m is determined to be 1276 m s^{-1} based on the Anderson formula (3) for an isotropic material.[53]

$$v_m = \left(\frac{1}{3}\left[\frac{2}{v_t^3} + \frac{1}{v_l^3}\right]\right)^{-1/3} \tag{3}$$

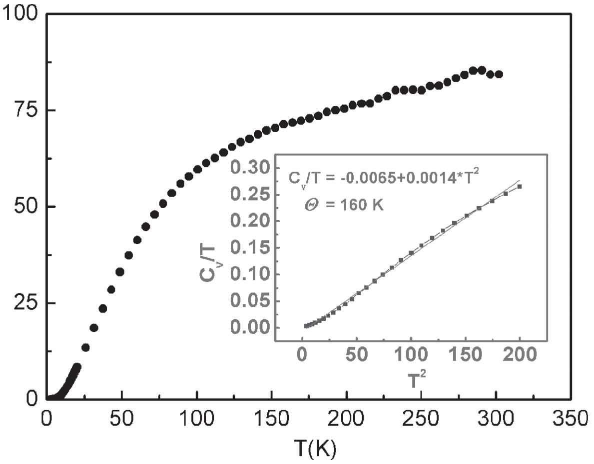

Figure 6. Low temperature C_v measurement and the fittings of a Debye temperature-based C_v curve, inset shows a calculation of the Debye temperature. The Debye temperature was fitted by $\frac{C_V}{T} = \frac{12NR\pi^4}{5\Theta^3}T^2$, here Θ is 160 for as-synthesized $MgAg_{0.97}Sb_{0.99}$ samples.

The low Debye temperature is typical for a material with weak chemical bonds. Here, within the Debye model, as shown in **Figure 6** and inset, we further confirmed the mean phonon velocity v_m. using the calculated Debye temperature from the measured specific heat (C_p) for as-synthesized α-$MgAg_{0.97}Sb_{0.99}$ phase via[54]

$$\Theta = \frac{v_m \hbar}{k_B}\left(\frac{6\pi^2}{V}\right)^{1/3} \tag{4}$$

where V is the average volume per atom calculated from the refined lattice parameters. The calculated Debye temperature is 160 K and average phonon velocity v_m 1500 m s^{-1} for as-synthesized α-$MgAg_{0.97}Sb_{0.99}$ sample. The latter value is very close to the measured value 1276 m s^{-1}. In comparison, the mean phonon velocity v_m. for other significant TE materials with intrinsic low thermal conductivity are 2310 m s^{-1} (β-Zn_4Sb_3),[8] SnSe (1422, 2002, 1814 m s^{-1} for *a*, *b*, *c*, axes, respectively),[9] 4800 m s^{-1} ($AgSbTe_2$),[10] and 2107 m s^{-1} (BiCuSeO).[55] Particularly, the low phonon velocity of 1120 m s^{-1} in the transverse lattice modes of α-$MgAg_{0.97}Sb_{0.99}$ is crucial, and similar situation can be found in the superionic conducting material such as Cu_2Se,[13,14] Cu_2S,[15] Cu_7PSe_6,[17] which shows significant softening of shear modes due to melt-like copper sublattice. We suggest that it is the softening transversal lattice modes that lead to the low lattice thermal conductivity in $MgAg_{0.97}Sb_{0.99}$, while concurrent Ag^+ and Mg^{2+} ion migrations being the dynamic origin. According to Cahill's formulation,[56]

$$k_{\min} = \frac{1}{2}\left(\frac{\pi}{6}\right)^{1/3} k_B V^{-2/3}(2v_t + v_l) \tag{5}$$

where V is the average volume per atom calculated from the refined lattice parameters, v_t and v_l are the transversal and longitudinal phonon velocity, respectively. An extremely low, $\kappa_{\min}$ of ≈ 0.42 W m^{-1} K^{-1} is obtained for as-synthesized α-$MgAg_{0.97}Sb_{0.99}$ sample. This is quite smaller than the measured value 0.78 W m^{-1} K^{-1} and implies that further suppression of lattice thermal conductivity could be achieved by increasing phonon scattering. The phonon mean free path can be calculated from the formula $k_L = \frac{1}{3}C_V v l$, where room temperature κ_L is 0.78 W m^{-1} K^{-1} and v is 1276 m s^{-1}, the phonon mean free path l is calculated to be ≈ 8.9 Å, which is even less than the lattice parameters. Therefore, instead of the scattering from nanocrystalline in as-synthesized $MgAg_{0.97}Sb_{0.99}$, we believe that phonon scatterings from alloy doping and other point defects would be promising strategies in the reduction of lattice thermal conductivity. Following this route, the total thermal conductivity of the heat-treated α-MgAg$_{0.97}$Sb$_{0.99}$ sample drops further to 0.81 W m^{-1} K^{-1}, and to 0.6 W m^{-1} K^{-1} for its lattice part. We believe that this is due to the phonon scattering by additional Ag and Sb vacancies as we have observed in the structural analysis. Moreover, this is in accordance with our previous work of Ni doping on the Ag site, which led to substantial reduction of lattice thermal conductivity compared to that of the undoped α-MgAg$_{0.97}$Sb$_{0.99}$.[23]

The temperature-dependent *ZT* curves for α-MgAg$_{0.97}$Sb$_{0.99}$ phases are shown in Figure 5d. Overall it can be seen that *ZT* increases with the increase of temperature and reaches the highest at 450 K. The heat-treated sample has higher *ZT*s than the as-synthesized sample in the temperature range between 250 and 450 K, mostly due to reduced thermal conductivity in this regime. This *ZT* feature can be utilized in real applications since the materials would always be subject to heating in operation. It should be noted that the α-MgAg$_{0.97}$Sb$_{0.99}$ phase is thermodynamically stable up to 575 K, beyond which α to β phase transition takes place.

3. Conclusions

In summary, we have disclosed the local atomic disorder induced by concurrent ion migrations between Ag sites and Mg sites in α-MgAgSb-based materials through XRD structure refinement, STEM, NMR experiments, and DFT calculations. This concurrent ion migration for two types of cations is very rare and has not been reported in any other thermoelectric material. The low activation energy of migrations for Ag^{+} and Mg^{2+} ions under nonequilibrium state in α-MgAgSb-based materials induced the softening transverse phonon modes, which is the leading reason for the low thermal conductivity in α-MgAgSb. In combination with the considerable hole mobility and moderate electrical transport properties, high *ZT* values in MgAgSb-based materials can be understood. Our findings demonstrate that concurrent ion migrations can play an important role in the reduction of thermal conductivity and may help in developing new materials for thermoelectric applications.

Experimental Section

Synthesis and X-Ray Diffraction Structural Refinement: A two-step process combining ball milling with hot pressing was used to synthesize the material. For the synthesis of MgAg$_{0.97}$Sb$_{0.99}$, 0.8102 g magnesium (Mg, Sigma–Aldrich, 99.8% metal basis) and 3.4877 g silver (Ag, Sigma–Aldrich, 99.9% metal basis) metal pieces (Mg:Ag = 1:0.97, atomic ratio) were first loaded into a stainless steel jar with balls inside the argon-filled glove box, followed by ball milling for 8 h leading to formation of Mg–Ag phase. Following this step, 4.0181 g of antimony (Sb, Sigma–Aldrich, 99.8% metal basis) chunks was added into the jar inside the glove box corresponding to atomic ratio of Mg:Ag:Sb = 1:0.97:0.99, with another ball milling of 5 h. The final powders were hot pressed under DC current at 575 K for 8 min. Figure S1 (Supporting Information) shows the SEM image and the elemental (Mg, Ag, and Sb) mapping images of the as-synthesized α-MgAg$_{0.97}$Sb$_{0.99}$ sample determined by SEM–EDX, which reveals that the sample is in pure phase and all the elements are homogeneously distributed in the bulk. In order to investigate the phase stability of the as-synthesized α-MgAg$_{0.97}$Sb$_{0.99}$ and its influence on the thermoelectric properties, the as-synthesized sample was heated from room temperature to 575 K and then cooled down to room temperature in Ar atmosphere. The obtained sample was referred to the heat-treated sample in the following text. Temperature-dependent powder XRD was collected on a PANalytical multipurpose diffractometer with an X'celerator detector (PANalytical X'Pert Pro) and Cu Kα radiation source. Based on the Rietveld method, FullProf.2k (version 5.40) program was used to perform the refinement against X-ray powder diffraction data of the as-synthesized and heat-treated samples. In the structure refinement for the as-synthesized sample, the atomic ratio was constrained to Mg:Ag:Sb = 1:0.97:0.99, which is consistent with its nominal and the lately analyzed compositions of MgAg$_{0.97}$Sb$_{0.99}$. The thermal displacement parameters of three Ag sites in Sb tetrahedrons were set to be the same because the sizes and chemical environments of three tetrahedrons are identical.

Thermoelectric Property Measurement Between Room Temperature and 575 K: Thermal diffusivity (*D*) and electrical transport measurements were performed on all samples. Thermal diffusivities (*D*) were measured by LFA447 (NETZSCH), the diameter of disc samples was 12 mm, with thickness of 1–2 mm, and coated by 10 µm amorphous carbon. Thermal conductivity above room temperature was calculated using $\kappa = D\rho C_p$, where ρ is the density of sample, *D* is the thermal diffusivity, and C_p is the specific heat. The density of the as-synthesized MgAg$_{0.97}$Sb$_{0.99}$ is 6.19 g cm^{-3}, ≈97% of the theoretical density of α-MgAg$_{0.97}$Sb$_{0.99}$. ZEM-3 (ULVAC-RIKO) and Linsis LRS-3 was used to measure the electrical transport properties for all samples with the sample dimensions of $2.5 \times 2.5 \times 11$ mm^3.

Low-Temperature Physical Property Measurement: The low temperature physical properties including electrical resistivity (ρ), Seebeck coefficient (*S*), thermal conductivity (κ), Hall coefficient (RH), and specific heat (C_p) were all measured on a Physical Property Measurement System (PPMS-9) from Quantum Design. Among these, the measurement of ρ (*T*) was performed by a standard four-point method, with applying a typical current of 1 mA. *S* (*T*) and κ (*T*) were determined by a continuous relaxation-time method with one heater and two thermometers in the thermal transport option (TTO), with a temperature gradient along the sample set to be 2% of the base temperature. The emissivity value used in the thermal transport measurement is 1. The measurement error is 5% below 150 K, and 10%–20% in the range of 150–300 K due to the increased radiation losses at elevated temperatures. The typical sample dimension was $1 \times 2 \times 5$ mm^3. The Hall coefficient R_H (*T*) was determined by using a four-contact technique and measuring the Hall resistivity in magnetic fields (here *B* = 5 *T*) of opposite directions to cancel out the resistive contribution. No obvious field dependence was found on the Hall effect. The specific heat below room temperature was measured by heat pulse relaxation technique in PPMS. The room temperature Hall coefficient measurement was performed on Accent HL5500 Hall System. The sample dimensions were $3 \times 3 \times 0.5$ mm^3, four-point method was used in the resistivity measurement. Within the one-band model, the charge-carrier concentration was determined by $n = 1/(e/|R_H|)$. The Hall mobility was determined by $\mu_H = |R_H|/\rho$.

Speed of Sound Measurements: The measurements were performed at room temperature to extract the longitudinal and transverse sound velocities, respectively. The data were obtained by use of a Panametrics NDT 5077PR squarewave pulser/receiver head; the response was recorded with a Tektronix TDS 2012C digital oscilloscope. Glycerin was used as a couplant between the sample and the ultrasonic transducer.

Scanning Transmission Electron Microscopy: STEM was performed on a JEM-ARM 200F transmission electron microscopy (JEOL, Japan) operating at 200 kV, equipped with a spherical aberration corrector (CEOS Gmbh) for the as-synthesized α-MgAg$_{0.97}$Sb$_{0.99}$ sample. STEM images were recorded with an HAADF detector (70–250 mrad) and ABF detector (11–25 mrad). The intensity of an atomic column in the HAADF imaging mode is proportional to $\approx Z^2$, where *Z* denotes atomic number.[57] The intensity of an atomic column in the ABF imaging mode is proportional to $\approx Z^{1/3}$.[58]

Nuclear Magnetic Resonance Measurement: ^{25}Mg NMR spectra were taken on a Bruker Ascend III 400 HD spectrometer with a spin-echo pulse sequence, and the Knight shifts were referenced to a 1 mol L^{-1} MgCl2 aqueous solution, respectively.

Density Functional Theory Calculations: The first-principles calculations presented in our work were performed using the DMol^3 program code[59,60] based on DFT. The GGA–PBE function[61] was adopted for the exchange-correlation potentials with all-electron for core treatment. The wave functions were expanded in terms of a double-numerical plus polarization (DNP) basis set with a global orbital cutoff of 4.9 Å. A Monkhorst Pack scheme[62] k-point mesh of $3 \times 3 \times 2$ in the reciprocal space was used for the conventional cells of α-MgAgSb. Atomic positions are fully relaxed with the lattice parameters fixed as experimental one a = 9.1687 Å and c = 12.7075 Å. The convergence tolerances of energy, force, and displacement were 1×10^{-5} Ha, 2×10^{-3} Ha Å^{-1}, and 5×10^{-3} Å, respectively. The self-consistent field was set as 5×10^{-6} eV atom^{-1}.

The conventional cells with 48 atoms were constructed as diffusion models of Ag and Mg migrations in α-MgAgSb. The linear synchronous transit (LST) and quadratic synchronous transit (QST) methods with conjugate gradient (CG) method refinements to search the transition state were performed.[63,64] The root mean square convergence of gradients was less than 2×10^{-3} Ha Å^{-1}. The diffusion model of Ag and Mg migrations was constructed with a conventional cell with 48 atoms, which were twice larger than the primitive cell. The lattice parameters a = 9.17 Å and c = 12.71 Å were near 10 Å, which was generally large enough to ignore the interaction between two adjacent cells. Moreover, it was found that there were few displacements of atoms near the edge of cell during Ag/Mg migration. Therefore, it was considered that the size of the conventional cell was enough to investigate the migration of constituent atoms in α-MgAgSb.

Molecular dynamics (MD) simulation was performed using CASTEP program code[50] and the GGA–PBE function[61] was adopted for the exchange-correlation potentials. A conventional cell with 48 atoms of α-MgAgSb was used for calculations. The simulation temperature was set to be 1000 K and simulation time is 5 ps with a step of 2 fs.

Supporting Information

Supporting Information is available from the Wiley Online Library or from the author.

Acknowledgements

Work in the Institute of Physics at the Chinese Academy of Sciences was supported by the startup package for young faculties and the MOST of China (Grant No: 2012CB921601). The work performed at University of Houston was supported by DOE under a contract number DE-FG02-13ER46917/DE-SC0010831. The authors greatly appreciate insightful discussions with Dr. Guangyao Liu on the XRD structural refinement, Mr. Xu Chen's contribution on data collection in Figure 1. The authors also thank Prof. Gang Chen and Dr. Sangyeop Lee from the Department of Mechanical Engineering at MIT for their contributions in the manuscript revision.

Received: July 21, 2015
Revised: August 19, 2015

---

[1] B. C. Sales, *Mater. Res. Soc. Bull.* **1998**, *23*, 15.
[2] K. F. Hsu, S. Loo, F. Guo, W. Chen, J. S. Dyck, C. Uher, T. Hogan, E. K. Polychroniadis, M. G. Kanatzidis, *Science* **2004**, *303*, 818.
[3] B. Poudel, Q. Hao, Y. Ma, Y. C. Lan, A. Minnich, B. Yu, X. Yan, D. Wang, A. Muto, D. Vashaee, X. Chen, J. Liu, M. S. Dresselhaus, G. Chen, Z. F. Ren, *Science* **2008**, *320*, 634.
[4] K. Biswas, J. He, I. D. Blum, C. I. Wu, T. P. Hogan, D. N. Seidman, V. P. Dravid, M. G. Kanatzidis, *Nature* **2012**, *489*, 414.
[5] J. P. Heremans, V. Jovovic, E. S. Toberer, A. Saramat, K. Kurosaki, A. Charoenphakdee, S. Yamanaka, G. J. Snyder, *Science* **2008**, *321*, 554.
[6] Y. Pei, X. Shi, A. LaLonde, H. Wang, L. Chen, G. J. Snyder, *Nature* **2011**, *473*, 66.
[7] W. Liu, X. Tan, K. Yin, H. Liu, X. Tang, J. Shi, Q. Zhang, C. Uher, *Phys. Rev. Lett.* **2012**, *108*, 16660.
[8] G. J. Snyder, M. Christensen, E. Nishibori, T. Caillat, B. B. Iversen, *Nat. Mater.* **2004**, *3*, 458.
[9] L. D. Zhao, S. H. Lo, Y. Zhang, H. Sun, G. Tan, C. Uher, C. Wolverton, V. P. Dravid, M. G. Kanatzidis, *Nature* **2014**, *508*, 373.
[10] D. T. Morelli, V. Jovovic, J. P. Heremans, *Phys. Rev. Lett.* **2008**, *101*, 035901.
[11] M. D. Nielsen, V. Ozolins, J. P. Heremans, *Energy Environ. Sci.* **2013**, *6*, 570.
[12] M. Ferhat, J. Nagao, *J. Appl. Phys.* **2000**, *88*, 15.
[13] H. L. Liu, X. Shi, F. F. Xu, L. L. Zhang, W. Q. Zhang, L. D. Chen, Q. Li, C. Uher, T. Day, G. J. Snyder, *Nat. Mater.* **2012**, *11*, 422.
[14] H. L. Liu, X. Yuan, P. Lu, X. Shi, F. F. Xu, Y. He, Y. S. Tang, S. Q. Bai, W. Q. Zhang, L. D. Chen, Y. Lin, L. Shi, H. Lin, X. Y. Gao, X. M. Zhang, H. Chi, C. Uher, *Adv. Mater.* **2013**, *25*, 6607.
[15] Y. He, T. Day, T. Zhang, H. Liu, X. Shi, L. Chen, G. J. Snyder, *Adv. Mater.* **2014**, *26*, 3974.
[16] Y. He, P. Lu, X. Shi, F. F. Xu, T. S. Zhang, G. J. Snyder, C. Uher, L. D. Chen, *Adv. Mater.* **2015**, *27*, 3639.
[17] K. S. Weldert, W. G. Zeier, T. W. Day, M. PanthÖfer, G. J. Snyder, W. Tremel, *J. Am. Chem. Soc.* **2014**, *136*, 12035.
[18] S. R. Brown, S. M. Kauzlarich, F. Gascoin, G. J. Snyder, *Chem. Mater.* **2006**, *18*, 1873.
[19] K. K. Kurosaki, A. Kosuga, H. Muta, M. Uno, S. Yamanaka, *Appl. Phys. Lett.* **2005**, *87*, 061919.
[20] J. S. Rhyee, K. H. Lee, S. M. Lee, E. Cho, S. Kim, E. Lee, Y. S. Kwon, J. H. Shim, G. Kotliar, *Nature* **2009**, *459*, 965.
[21] Q. Jie, H. Wang, W. Liu, H. Wang, G. Chen, Z. F. Ren, *Phys. Chem. Chem. Phys.* **2013**, *15*, 6809.
[22] M. J. Kirkham, A. M. Santos, C. J. Rawn, E. Lara-Curzio, J. W. Sharp, A. J. Thompson, *Phys. Rev. B* **2012**, *85*, 144120.
[23] H. Zhao, J. H. Sui, Z. Tang, Y. C. Lan, Q. Jie, D. Kraemer, K. McEnaney, A. Guloy, G. Chen, Z. F. Ren, *Nano Energy* **2014**, *7*, 97.
[24] J. Shuai, H. S. Kim, Y. C. Lan, S. Chen, Y. Liu, H. Zhao, J. H. Sui, Z. F. Ren, *Nano Energy* **2014**, *11*, 640.
[25] J. H. Sui, J. Shuai, Y. C. Lan, Y. Liu, R. He, D. Z. Wang, Q. Jie, Z. F. Ren, *Acta Mater.* **2015**, *87*, 266.
[26] P. Z. Ying, X. H. Liu, C. G. Fu, X. Q. Yue, H. H. Xie, X. B. Zhao, W. Q. Zhang, T. Zhu, *J. Chem. Mater.* **2015**, *27*, 909.
[27] D. Kraemer, J. H. Sui, K. McEnaney, H. Zhao, Q. Jie, Z. F. Ren, G. Chen, *Energy Environ. Sci.* **2015**, *8*, 1299.
[28] S. Nakamura, T. Maeda, T. Wada, *Phys. Status Solidi A* **2013**, *7*, 1317.
[29] S. Nakamura, T. Maeda, T. Wada, *Jpn. J. Appl. Phys.* **2013**, *52*, 04CR01.
[30] Y. Mo, S. P. Ong, G. Ceder, *Chem. Mater.* **2014**, *26*, 5208.
[31] K. Kang, D. Morgan, G. Ceder, *Phys. Rev. B* **2009**, *79*, 014305.
[32] G. K. P. Dathar, D. Sheppard, K. J. Stevenson, G. Henkelman, *Chem. Mater.* **2011**, *23*, 4032.
[33] F. Gascoin, A. Maignan, *Chem. Mater.* **2011**, *23*, 2510.
[34] H. Liu, X. Shi, M. Kirkham, H. Wang, Q. Li, C. Uher, W. Zhang, L. Chen, *Mater. Lett.* **2013**, *93*, 121.
[35] W. J. Qiu, L. L. Xi, P. Wei, X. Z. Ke, J. H. Yang, W. Q. Zhang, *Proc. Natl. Acad. Sci USA* **2014**, *111*, 15031.
[36] D. Y. Chung, T. Hogan, P. Brazis, M. Rocci-Lane, C. Kannewurf, M. Bastea, C. Uher, M. G. Kanatzidis, *Science* **2000**, *287*, 1024.
[37] R. Mohanraman, R. Sankar, K. M. Boopathi, F. C. Chou, C. W. Chu, C. H. Lee, Y. Y. Chen, *J. Mater. Chem. A* **2014**, *2*, 2839.
[38] T. Caillat, J. P. Fleurial, A. Borshchevsky, *J. Phys. Chem. Solids* **1997**, *58*, 1119.

[39] J. Androulakis, K. F. Hsu, R. Pcionek, H. Kong, C. Uher, J. J. D'Angelo, A. Downey, T. Hogan, M. G. Kanatzidis, *Adv. Mater.* **2006**, *18*, 1170.
[40] E. S. Toberer, C. A. Cox, S. R. Brown, T. Ikeda, A. F. May, S. M. Kauzlarich, G. F. Snyder, *Adv. Funct. Mater.* **2008**, *18*, 2795.
[41] X. Yan, W. Liu, S. Chen, H. Wang, Q. Zhang, G. Chen, Z. F. Ren, *Adv. Energy Mater.* **2013**, *3*, 1195.
[42] C. G. Fu, T. J. Zhu, Y. T. Liu, H. H Xie, X. B. Zhao, *Energy Environ. Sci.* **2015**, *8*, 216.
[43] G. Joshi, H. Lee, Y. Lan, X. Wang, G. Zhu, D. Wang, R. W. Gould, D. C. Cuff, M. Y. Tang, M. S. Dresselhaus, G. Chen, Z. F. Ren, *Nano Lett.* **2008**, *8*, 4670.
[44] H. Nowotny, W. Sibert, *Z. Metallkd.* **1941**, *33*, 391.
[45] R. T. B. Frost, G. V. Raynor, *Proc. R. Soc. London* **1950**, *A203*, 132.
[46] D. A. Keen, S. Hull, *J. Phys.: Condens. Matter* **1998**, *10*, 8217.
[47] D. Aurbach, Z. Lu, A. Schechter, Y. Gofer, H. Gizbar, R. Turgeman, Y. Cohen, M. Moshkovich, E. Lev, *Nature* **2000**, *407*, 724.
[48] E. Sheha, *Int. J. Electrochem. Sci.* **2013**, *8*, 3653.
[49] M. Kusakabe, Y. Shirakawa, S. Tamaki, Y. Ito, *J. Phys. Soc. Jpn.* **1994**, *64*, 170.
[50] S. J. Clark, M. D. Segall, C. J. Pickard, P. J. Hasnip, M. J. Probert, K. Refson, M. C. Payne, *Z. Kristallogr.* **2005**, *220*, 567.
[51] D. Massiot, F. Fayon, M. Capron, L. King, S. L. Calvé, B. Alonso, J. Durand, B. Bujoli, G. Hoatson, *Magn. Reson. Chem.* **2002**, *40*, 70.
[52] V. I. Fistul, *Heavily Doped Semiconductors*, Plenum Press, New York **1969**.
[53] G. Slack, *Solid State Phys.* **1979**, *34*, 1.
[54] O. Anderson, *J. Phys. Chem. Solids* **1963**, *24*, 909.
[55] L. D. Zhao, J. He, D. Berardan, Y. Lin, J. F. Li, C. W. Nan, N. Dragoe, *Energy Environ. Sci.* **2014**, *7*, 2900.
[56] D. G. Cahill, S. K. Watson, R. O. Pohl, *Phys. Rev. B* **1992**, *46*, 6131.
[57] S. J. Pennycook, L. A. Boatner, *Nature* **1988**, *336*, 565.
[58] S. D. Findlay, N. Shibata, H. Sawada, E. Okunishi, Y. Kondo, Y. Ikuhara, *Ultramicroscopy* **2010**, *110*, 903.
[59] B. Delley, *J. Chem. Phys.* **1990**, *92*, 508.
[60] B. Delley, *J. Chem. Phys.* **2000**, *113*, 7756.
[61] J. P. Perdew, K. Burke, M. Ernzerhof, *Phys. Rev. Lett.* **1996**, *77*, 3865.
[62] H. J. Monkhorst, J. D. Pack, *Phys. Rev. B* **1976**, *13*, 5188.
[63] T. A. Halgren, W. N. Lipscomb, *Chem. Phys. Lett.* **1977**, *49*, 225.
[64] N. Govind, M. Petersen, G. Fitzgerald, D. King-Smith, J. Andzelm, *Comput. Mater. Sci.* **2003**, *28*, 250.